ACS OMEGA

http://pubs.acs.org/journal/acsodf

Article

High-Capacity Anode Material for Lithium-Ion Batteries with a Core–Shell $NiFe_2O_4$/Reduced Graphene Oxide Heterostructure

Chang Liu, Tong Zhang, Lixin Cao, and Kun Luo*

Cite This: *ACS Omega* 2021, 6, 25269–25276

Read Online

ACCESS | Metrics & More | Article Recommendations | Supporting Information

ABSTRACT: A novel composite consisting of transition-metal oxide and reduced graphene oxide (rGO) has been designed as a highly promising anode material for lithium-ion batteries (LIBs). The anode material for LIBs exhibits high-rate capability, outstanding stability, and nontoxicity. The structural characterization techniques, such as X-ray diffraction, Raman spectra, and transmission electron microscopy, indicate that the material adopts a unique core–shell structure with $NiFe_2O_4$ nanoparticles situated in the center and an rGO layer coated on the surface of $NiFe_2O_4$ particles (denoted as $NiFe_2O_4$/rGO). The $NiFe_2O_4$/rGO material with a core–shell structure exhibits an excellent electrochemical performance, which shows a capacity of 1183 mA h g^{-1} in the first cycle and maintains an average capacity of ∼1150 mA h g^{-1} after 900 cycles at a current density of 500 mA g^{-1}. This work provides a broad field of vision for the application of transition-metal-oxide materials in electrodes of lithium-ion batteries, which is of great significance for further development of lithium-ion batteries with excellent performance.

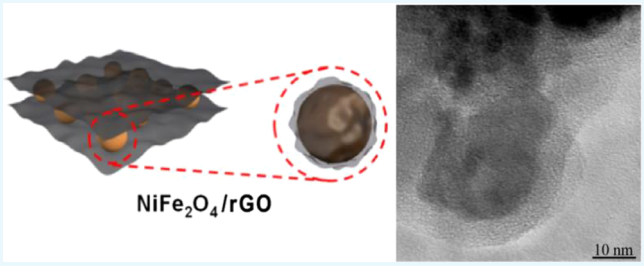

1. INTRODUCTION

As human beings increasingly rely on various types of energy-driven equipment, researchers have paid more attention to the evolution of energy storage and conversion devices.[1−4] Lithium-ion batteries (LIBs) are one of the most competitive systems because of their high theoretical capacity, security, low cost, nontoxicity, etc.[5,6] Although LIBs with a graphite anode that have been commercialized show low operating voltage and outstanding cycling stability, a low theoretical capacity of about 372 mA h g^{-1} of graphite is far below the demand of large facilities.[7−9] Therefore, exploring a new anode material with higher capacity and better structural stability is a priority.

Transition-metal oxides (TMOs) have been proved to be very promising anode materials because they can deliver reversible capacities almost 3 times higher than the specific capacity of graphite materials, as well as for their low cost.[10] However, transition-metal-oxide materials exhibit poor rate capability and drastic capacity fading because of low conductivity and large volume expansion during cycling. Various strategies have often been applied to solve these problems. The particle size of TMOs can be controlled through a series of chemical methods, promoting electrochemical processes and maintaining structural integrity.[11−14] Carbon materials can also be introduced to fabricate composites, which can buffer the volume expansion of TMOs during the cycling and increase electronic conductivity.[15−17] Graphene oxide (GO)/MoS_3 has been prepared through a facile method that shows the highest specific capacity of 685 mA h g^{-1} after 1000 cycles at 2 A g^{-1}.[18] In addition, materials with nanostructures such as a hollow structure or a core–shell structure through material engineering can achieve excellent electrochemical performances. For example, core–shell porous nanocubic Mn_2O_3/TiO_2, which was synthesized as a high-performance anode for LIBs, achieved a cycling capacity of 936 mA h g^{-1} after 100 cycles at a charging/discharging rate of 200 mA g^{-1}.[19]

Among various TMO anode materials, $NiFe_2O_4$ has been considered as an appealing electrode material for LIBs because of high theoretical capacity (915 mA h g^{-1}). Previous studies have reported a reversible capacity of ∼900 mA h g^{-1} exhibited by the $NiFe_2O_4$ anode material.[20,21] The Coulombic efficiency is as low as 34.8 and 98.5% for the 1st and 30th cycles, respectively.[22] However, similar to other TMOs, the $NiFe_2O_4$ anode material also exhibits poor electronic conductivity and fast capacity fading during cycling.[23] To overcome these insufficiencies, structural and morphological modifications on oxide materials were carried out by researchers.[24−26] A hollow $NiFe_2O_4$ material exhibits a stable discharge capacity of 840–850 mA h g^{-1} at a current density of 200 mA g^{-1}.[24] $NiFe_2O_4$ nanofibers exhibit an outstanding capacity of 1000 mA h g^{-1} after 100 cycles with a high Coulombic efficiency of 100%.[25] The sandwich-structured graphene–$NiFe_2O_4$–carbon nano-

Received: June 9, 2021
Accepted: September 10, 2021
Published: September 23, 2021

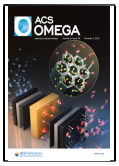

composite has been prepared via a hydrothermal method, followed by carbon coating, which exhibits an exceptional cycle stability of 1195 mA h g^{-1} after 200 cycles at 500 mA g^{-1}.[26]

In this study, we successfully synthesized a $NiFe_2O_4$/reduced graphene oxide (rGO) composite with a core−shell structure via a facile chemical process. The as-prepared $NiFe_2O_4$ material adopts a particle size of 18−20 nm, which is beneficial for the participation of $NiFe_2O_4$ in electrochemical reactions. The rGO network is considered to serve as a conductor of electrons and provide pathways for Li-ion diffusion to improve the electronic and ionic conductivities. More importantly, rGO on the surface of $NiFe_2O_4$ could act as a protective layer to form a unique core−shell structure, which can ease the volume changes of $NiFe_2O_4$ during cycling. Therefore, as an anode material for LIBs, the $NiFe_2O_4$/rGO composite exhibits improved lithium-storage performances. After 900 cycles, the $NiFe_2O_4$/rGO composite still exhibits an average capacity of ∼1150 mA h g^{-1} at 500 mA g^{-1}. The findings provide wide insights into the utilization of transition-metal-oxide materials for electrodes in lithium-ion batteries, which is of vital importance to further developing LIBs with excellent performances.

2. RESULTS AND DISCUSSION

The fabrication method of the $NiFe_2O_4$/rGO composite utilized in this study is schematically illustrated in Figure 1.

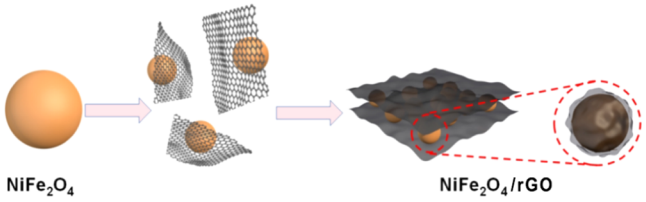

Figure 1. Schematic illustration of the synthesis process of $NiFe_2O_4$/rGO.

Transition-metal nitrate and citric acid were mixed and heated to obtain $NiFe_2O_4$. $NiFe_2O_4$ and reduced graphene oxide (rGO) were then placed in ethanol for an ultrasonic process before a hydrothermal reaction. The $NiFe_2O_4$/rGO composite with a core−shell structure was prepared through a self-assembly treatment using a hydrothermal method.

The structural information of the $NiFe_2O_4$/rGO material was characterized by X-ray diffraction (XRD). Figure 2a shows the XRD patterns of $NiFe_2O_4$ and the $NiFe_2O_4$/rGO composite. In the representative XRD pattern, all of the diffraction peaks can be well indexed to the cubic inverse spinel-type $NiFe_2O_4$ (JCPDS card No. 54-0964). These characteristic diffraction peaks of $NiFe_2O_4$ at 18.428, 35.701, 37.320, 37.630, 43.383, 53.814, 57.293, and 63.021° correspond to the crystal planes of (111), (220), (311), (222), (400), (422), (511), and (440). The formation of a pure compound can be confirmed as no other phases or impurity peaks could be found. In addition, the XRD pattern of the $NiFe_2O_4$/rGO composite is similar to that of $NiFe_2O_4$ and all of the characteristic peaks of $NiFe_2O_4$ are well preserved, indicating that the $NiFe_2O_4$ phase was maintained intact in the chemical reaction where the rGO material was deposited on the surface of $NiFe_2O_4$. A new broad peak appears at about 26° for the $NiFe_2O_4$/rGO composite, which corresponds to the (002) characteristic peak of rGO. The structure of $NiFe_2O_4$/

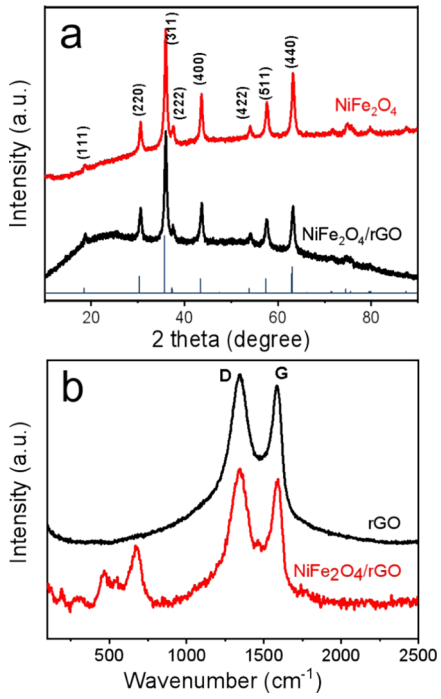

Figure 2. XRD patterns of $NiFe_2O_4$/rGO (black line) and $NiFe_2O_4$ (red line) (a), and Raman spectra of $NiFe_2O_4$/rGO (red line) and rGO (black line) (b).

rGO was also determined by Raman spectroscopy, as shown in Figure 2b. The Raman spectrum of the rGO exhibits two peaks at 1346 and 1582 cm^{-1}, which represent the D and G modes of amorphous carbon, respectively. The D band corresponds to the presence of defects, and the G band indicates ideal graphitic sp^2 carbons.[27−29] The ratio of D and G band intensities (I_D/I_G) is considered to indicate the degree of disorder in a carbon structure. As shown in Figure 2b, the I_D/I_G ratio of $NiFe_2O_4$/rGO is 1.10. This result indicates that rGO has a lower degree of graphitization, which is conducive to the intercalation and diffusion of Li^+ ions.[29−31] On comparing the Raman spectra of $NiFe_2O_4$ and $NiFe_2O_4$/rGO, there are some other peaks recognized for $NiFe_2O_4$/rGO in the range of 400−700 cm^{-1}, which were attributed to the spinel structure of $NiFe_2O_4$.[32,33] The $T_{2g(1)}$ mode at 191 cm^{-1} corresponds to the translational drive of the tetrahedron, in which the Ni/Fe metal cations are tetrahedrally coordinated with oxygen atoms. At 319 cm^{-1}, the E_g mode is related to the symmetric bending of the oxygen anions with respect to the Ni/Fe metal cations.[31] The $T_{2g(2)}$ mode at 478 cm^{-1} is considered to be the asymmetric stretching of the Fe/Ni and O bond at octahedral sites, while the $T_{2g(3)}$ mode at 546 cm^{-1} is the result of the asymmetric bending of oxygen anions with tetrahedral and octahedral metal cations.[32] The A_{1g} mode at 606 cm^{-1} belongs to the symmetric stretching of oxygen anions along Ni−O and Fe−O bonds, as shown Figure S1.[34,35]

The X-ray photoelectron spectroscopy (XPS) of $NiFe_2O_4$/rGO was carried out to study the chemical states of transition-metal cations, as shown in Figure 3. The Ni 2p spectrum shows two characteristic peaks at 855.1 and 872.5 eV and two satellites peaks at 862.0 and 878.0 eV owing to Ni 2p1/2 and Ni 2p3/2,[36] which imply that Ni exists as Ni^{2+}.[37] The characteristic peaks of the Fe 2p spectrum at 713.2 and 726.9 eV are attributed to Fe 2p3/2 and Fe 2p1/2, and there are two satellites peaks at 718.2 and 733.1 eV.[36,38] These signs confirm

https://doi.org/10.1021/acsomega.1c03050
ACS Omega 2021, 6, 25269−25276

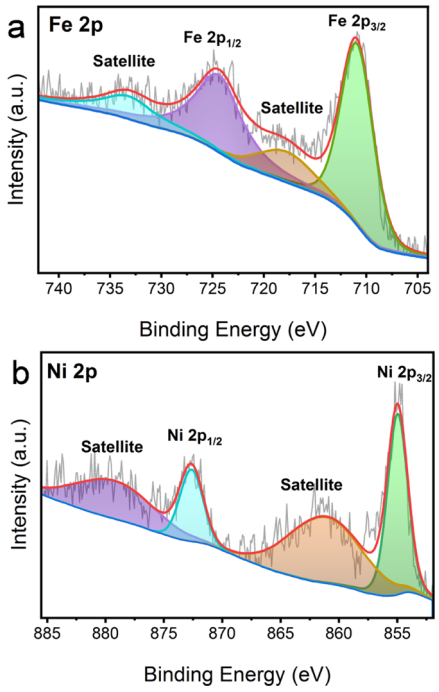

Figure 3. Fe 2p high-resolution XPS spectra of $NiFe_2O_4$/rGO (a), and Ni 2p high-resolution XPS spectra of $NiFe_2O_4$/rGO (b).

the existence of Fe^{3+} ions in the composite. The results of the XPS spectra correspond well to the observations in the XRD pattern of the composite, indicating the formation of the $NiFe_2O_4$ phase. The thermogravimetric analysis (TGA) curve for $NiFe_2O_4$/rGO is shown in Figure S2, which is tested in the range of 50−600 °C at the rate of 5 °C/min in air. Graphene burns at a temperature between 400 and 600 °C in air.[14] Therefore, the $NiFe_2O_4$/rGO nanocomposite is composed of ∼10 wt % rGO and ∼90 wt % $NiFe_2O_4$.

The morphology of the $NiFe_2O_4$/rGO composite has been determined by transmission electron microscopy (TEM). Figures S3a−c show the TEM images of $NiFe_2O_4$. The $NiFe_2O_4$ nanoparticles show an average size of 20 nm. Such a small particle renders more contact area between the anode and the electrolyte, thus improving the participation of $NiFe_2O_4$ in electrochemical process. The selected area electron diffraction (SAED) pattern of $NiFe_2O_4$ (Figure S3d) shows a ring-like diffraction pattern, revealing a polycrystalline structure of $NiFe_2O_4$. Figure 4 shows the HRTEM images of $NiFe_2O_4$/rGO at low and high magnifications. Compared with Figure 4c, it is obviously shown in Figure 4d that the $NiFe_2O_4$ particles are embedded in rGO and there is a shell with a thickness of ∼5 nm coating on the surface of $NiFe_2O_4$ particles, confirming the formation of a core−shell-structured $NiFe_2O_4$/rGO. Figure 4e exhibits a ring-like diffraction pattern, which could reveal the polycrystalline structure of $NiFe_2O_4$/rGO. As shown in Figure 4f, all small grains show a single-crystal structure, with obvious crystal lattice fringes. The crystal plane spacing is 0.294 nm, corresponding to the (220) plane of spinel $NiFe_2O_4$. The element distribution in the core−shell structure of $NiFe_2O_4$/rGO is also demonstrated by the energy-dispersive X-ray spectroscopy (EDS), as shown in Figure 4. It can be definitely observed from the distribution of Ni, Fe, O, and C elements that Ni, Fe, and O atoms are uniformly concentrated in the center of the particles, confirming the existence of the $NiFe_2O_4$ phase, whereas the C atoms are dominantly situated on the circumference of the particles, which undoubtedly indicates the formation of a heterogeneous core−shell $NiFe_2O_4$/rGO structure observed in Figure 4d.

To explore the electrochemical performances of core−shell $NiFe_2O_4$/rGO, a cyclic voltammetry (CV) test was conducted. The CV curves of the initial four cycles are shown in Figure 5a, which has been tested at a scan rate of 0.2 mV s^{-1} at the potential window of 0.01−3.00 V vs Li/Li^+. The cathodic peak of the first cycle started at 0.75 V, which is related to the formation of a solid−electrolyte interface (SEI) film and the reduction of $NiFe_2O_4$ during the first discharging process (eq 1).[39] The weak wide peak at about 1.5 V may be the result of insertion of Li^+ ions into the $NiFe_2O_4$/rGO electrode. The two broad anodic peaks at 1.6 and 1.8 V are attributed to the formation of NiO and Fe_2O_3 according to eqs 2 and 3 in the subsequent anodic scans, respectively.[27,40,41] After one cycle, all reduction peaks moved slightly toward a higher potential, implying that there was a loss of capacity because of the formation of the irreversible phase in the first cycle.[42] Meanwhile, the CV curves of $NiFe_2O_4$/rGO in the second and third cycles almost overlap, indicating the excellent reversibility of the electrochemical reactions.

$$NiFe_2O_4 + 8Li^+ + 8e^- \rightarrow Ni + 2Fe + 4Li_2O \quad (1)$$

$$Ni + Li_2O \rightarrow NiO + 2Li^+ + 2e^- \quad (2)$$

$$2Fe + 3Li_2O \rightarrow Fe_2O_3 + 6Li^+ + 6e^- \quad (3)$$

The charge/discharge curves of $NiFe_2O_4$/rGO were obtained between 0.01 and 3.00 V at 500 mA g^{-1}. As shown in Figure 5b, the initial charge−discharge curves exhibit two obvious plateaus at 1.70 and 0.75 V, which correspond well to the above CV results. The discharge plateau was replaced by a slope from 1.00 to 0.80 V in the subsequent cycle, corresponding to the irreversible reaction such as the formation of an SEI film. Furthermore, the charge/discharge platform is well maintained with the same shape after 50 cycles, indicating the outstanding reversibility of electrochemical reaction.

Figure 5c shows electrochemical impedance spectra of $NiFe_2O_4$ and $NiFe_2O_4$/rGO. All of the Nyquist plots consist of a slope line and a semicircle. The slope line is related to the Li^+ diffusion in the fibrous framework (Z_w), and the semicircle corresponds to the charge-transfer resistance (R_{ct}).[43] The fitted results show that the R_{ct} (54 Ω) of the $NiFe_2O_4$/rGO electrode is much lower than that of the $NiFe_2O_4$ electrode (154 Ω) and the diffusion coefficient of $NiFe_2O_4$/rGO (1.42×10^{-12} cm^2 s^{-1}) is higher than that of pure $NiFe_2O_4$ (6.64×10^{-13} cm^2 s^{-1}), which indicates that the electronic conductivity and ion mobility of the composite can be improved by coating rGO on $NiFe_2O_4$. Figure 5g shows the cycling performance of $NiFe_2O_4$/rGO at 500 mA g^{-1}. The $NiFe_2O_4$/rGO anode shows a first discharge capacity of 1183 mA h g^{-1}, which is much larger than the reversible capacity (∼900 mA h g^{-1}) reported previously.[20,21] The excess capacity may be related to the formation of SEI at the electrode/electrolyte interface caused by electrolyte reduction. The exposed vacancy defects of rGO also render more Li storage, resulting in extra capacity contribution.[44] In addition, excess oxygen in the anode could also react with some lithium, leading to extra capacity.[28,45] The first charge capacity is 842 mA h g^{-1} with a low Coulombic efficiency of 71.2%. The loss of capacity during charge process

https://doi.org/10.1021/acsomega.1c03050
ACS Omega 2021, 6, 25269−25276

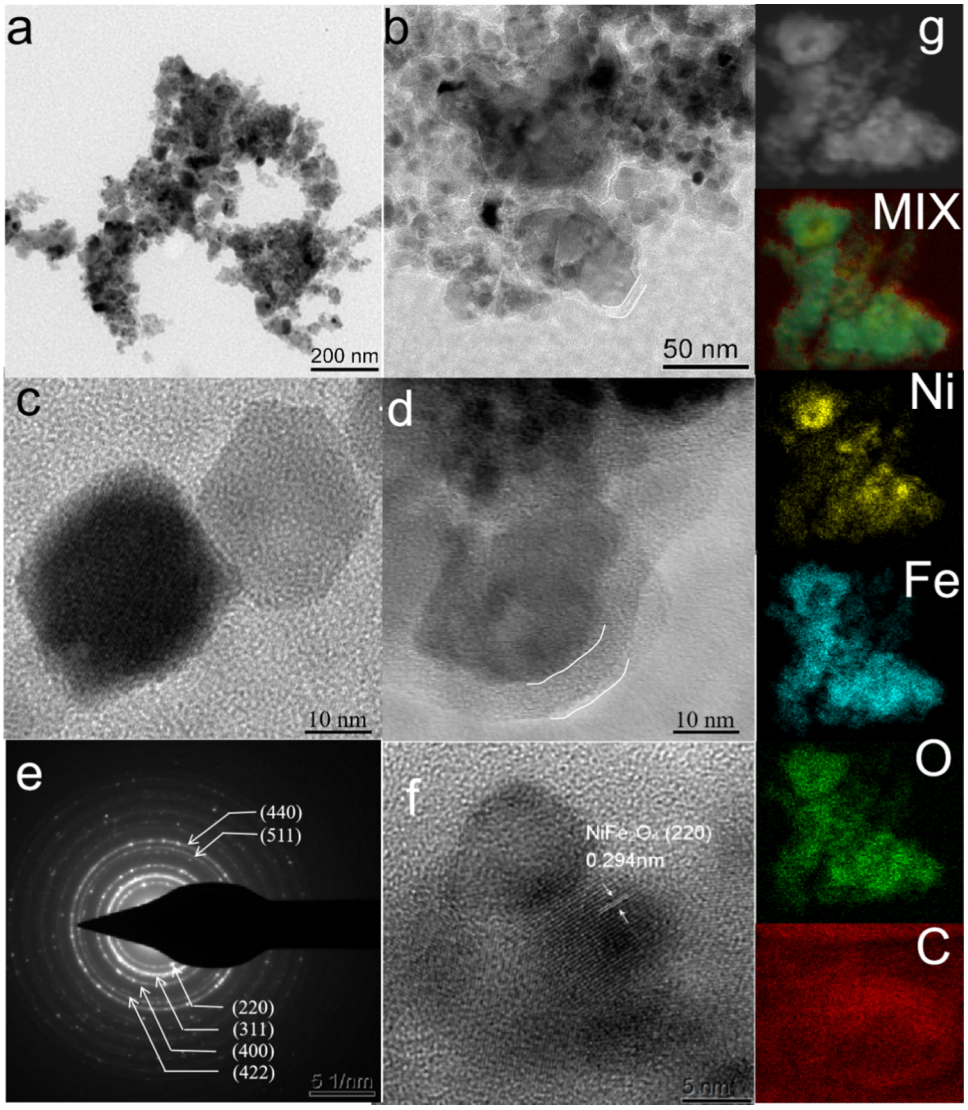

Figure 4. TEM images of $NiFe_2O_4$/rGO (a, b, and d); TEM image of $NiFe_2O_4$ (c); SAED pattern of $NiFe_2O_4$/rGO (e); HRTEM image of $NiFe_2O_4$/rGO (f); from top to bottom: elemental mapping images showing the elemental distribution of Ni, Fe, O, and C and the overlapped image (g).

can be attributed to the irreversible decomposition of the SEI and the incomplete conversion reaction.[45,46]

However, there is a drastic capacity fading of $NiFe_2O_4$/rGO during the initial 85 cycles due to the practical structural destruction caused by electrolytic grinding during the cycle, which was observed previously in the $NiFe_2O_4$-based anode material.[28,40] In subsequent cycles, the reversible capacity of the $NiFe_2O_4$ electrode gradually increases, which may be attributed to the formation of the SEI film and activation of $NiFe_2O_4$/rGO during the lithium insertion/extraction process.[45] After 900 cycles, a relatively stable reversible capacity of ~1150 mA h g^{-1} could be achieved with the Coulombic efficiency close to 100%, indicating the stabilization of the SEI film between the electrode and the electrolyte.[40,45] Figure S5 exhibits the cycling performance of $NiFe_2O_4$. A stable capacity of 105 mA h g^{-1} has been observed after a fast capacity fading. Compared to the $NiFe_2O_4$ electrode, the $NiFe_2O_4$/rGO electrode exhibits improved cycling performance. The enhanced cycling stability of $NiFe_2O_4$/rGO could be attributed to the following two reasons: (1) rGO as a shell layer can adapt to the volume change during the cycling process and alleviate the pulverization and aggregation of $NiFe_2O_4$; (2) the rGO network can effectively increase the electronic conductivity of $NiFe_2O_4$, facilitating the rapid transfer of electrons.[47,48]

Figure 5d shows the CV diagrams at different scan rates (0.2 to 1.8 mV s^{-1}). With increase in the scan rate, the intensity of peaks at 0.75 and 1.70 V increases. In addition, the oxidation peak moves toward a higher voltage and the reduction peak moves toward a lower voltage with increase of the scan rate, indicating the higher electrochemical polarization for $NiFe_2O_4$/rGO. The Nyquist plots of the $NiFe_2O_4$/rGO nanoparticles after different cycles (the 1st and the 20th) are shown in Figure 5f. On comparing the Nyquist plots of the $NiFe_2O_4$/rGO composite after cycles, the R_{ct} value increases from 17 Ω for the initial electrode to 54 Ω for the 20th cycle. The diffusion coefficients of $NiFe_2O_4$/rGO (initial) and $NiFe_2O_4$/rGO (after 20 cycles) are 1.42×10^{-12} and 5.24×10^{-11} cm^2 s^{-1}, respectively. This drastic change may be attributed to the activation of electrode materials and enhanced transport properties of $NiFe_2O_4$/rGO. In combination with the results of the cycling performance, this trend in

https://doi.org/10.1021/acsomega.1c03050
ACS Omega 2021, 6, 25269−25276

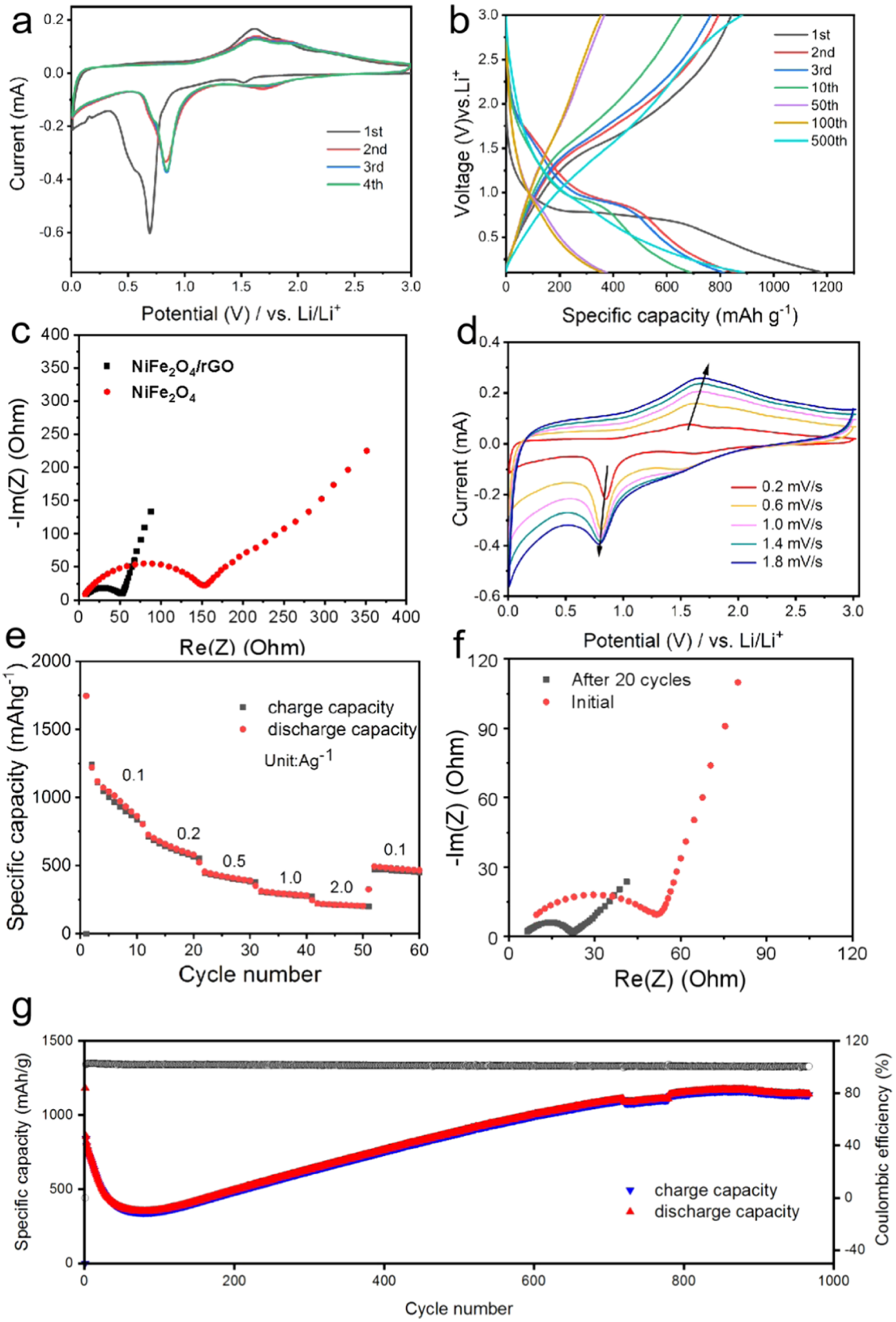

Figure 5. (a) Cyclic voltammetry curves of the $NiFe_2O_4$/rGO electrode. Scan rate: 0.2 mV s^{-1}; voltage range: 0.01−3.00 V. (b) Galvanostatic charge/discharge profiles of the $NiFe_2O_4$/rGO electrode. Voltage range: 0.01−3.00 V; current density: 500 mA g^{-1}. (c) Nyquist plots of the $NiFe_2O_4$ (red) and $NiFe_2O_4$/rGO (black) electrodes. (d) CV curves of the $NiFe_2O_4$/rGO electrode at different scan rates. (e) Rate capabilities of $NiFe_2O_4$/rGO. (f) Nyquist plots of $NiFe_2O_4$/rGO at the 1st and 20th cycles. (g) Charge/discharge capacity and Coulombic efficiency of the $NiFe_2O_4$/rGO electrode at 500 mA g^{-1}.

https://doi.org/10.1021/acsomega.1c03050
ACS Omega 2021, 6, 25269−25276

resistance is attributed to the formation of the SEI layer and the activation of $NiFe_2O_4$.

To further study the rate capacity of the $NiFe_2O_4$/rGO electrode, the electrode has been evaluated at different rates, as shown in Figure 5e. At a rate of 0.1 A g^{-1}, the discharge capacity reaches ~1745.8 mA h g^{-1}. At high rates of 0.2, 0.5, 1, and 2 A g^{-1}, the discharge capacities still remain at values of 804.2, 553.2, 376.3, and 272.4 mA h g^{-1}, respectively. The discharge capacity of 467.9 mA h g^{-1} was recovered when the rate was returned to 0.1 A g^{-1}. These results show that the $NiFe_2O_4$/rGO composite with a core−shell structure has great potential as a high-rate anode material for LIBs.

3. CONCLUSIONS

In conclusion, the $NiFe_2O_4$/rGO composite with a unique core−shell structure has been successfully prepared through a facile chemical process. The $NiFe_2O_4$/rGO electrode exhibits excellent cycling and rate performances as an anode material for LIBs. The rGO coating layer on the surface can not only benefit for the increase of electronic conductivity but also suppress the volume change during the charge/discharge processes. The introduction of the rGO layer onto $NiFe_2O_4$ provides an exceptional specific capacity of ~1150 mA h g^{-1} after 900 cycles at 500 mA g^{-1} with a high Coulombic efficiency of 100%, which is significantly improved when compared with that of $NiFe_2O_4$ nanoparticles. The EIS measurements show that the charge-transfer resistance of core−shell $NiFe_2O_4$/rGO is smaller than that of the $NiFe_2O_4$ nanoparticles. The excellent lithium-storage properties of the core−shell $NiFe_2O_4$/rGO electrode may be ascribed to the core−shell structure and the small size of $NiFe_2O_4$ particles, which can effectively improve the electronic conductivity of the electrodes and accommodate the change of volume during the lithium-ion insertion/extraction process. Thus, the $NiFe_2O_4$/rGO composite has great potential in the development of Li-ion batteries.

4. EXPERIMENTAL SECTION

4.1. Material Synthesis. In the preparation process, 4.08 g of $Fe(NO_3)_3{\cdot}9H_2O$, 1.10 g of $Ni(Ac)_2{\cdot}9H_2O$, and 3.04 g of anhydrous citric acid were dissolved in 20 ml of anhydrous ethanol solution and stirred at room temperature for 0.5 h. Then, the reaction mixture was continuously stirred for 2 h at 60 °C and then heated at 110 °C for 24 h to obtain a homogeneous mixture. $NiFe_2O_4$ was obtained by placing the mixture in a muffle oven at 5 °C min^{-1} to 450 °C for 5 h. Reduced graphene oxide (rGO) purchased from Alab (Shanghai) Chemical Technology Company (thickness: <1 nm; diam: 1−100 μm) was placed in 20 ml ethanol according to the proportion of ultrasonic for 1 h. The mixture was placed in a Teflon high-pressure reactor for hydrothermal reaction at 180 °C for 12 h. The product was washed with ethanol three times and dried in 60 °C for 24 h.

4.2. Material Characterization. The microstructures and morphologies of the materials were determined using a transmission electron microscope (TEM, JEM, 2011F). The crystal structures were evaluated using a powder X-ray diffraction (XRD) meter (Smart Lab 9KW) with Cu Kα radiation. Raman spectroscopy was performed using a Thermo DXR Microscope with 532 nm excitation laser wavelength. PHI 5000 Versa Probe, ULVAC-PHI with an Al Kα X-ray source (1486.6 eV), was used to measure X-ray photoelectron spectroscopy (XPS). The TGA curves were obtained using a SHIMADZU DTG-60H thermo balance in air with a 5 °C min^{-1} heating rate from 50 to 600 °C.

4.3. Electrochemical Measurements. Active materials, super P, and poly(vinylidene fluoride) (PVDF) (weight ratio: 8:1:1) were mixed in NMP to obtain a slurry. Then, the slurry was coated onto the Cu foil and dried at 80 °C for 12 h in a vacuum oven. The electrolyte was 1.0 M solution of $LiPF_6$ in the mixture of EC/DEC (1:1 by volume). The cells were assembled in a glovebox filled with Ar. The galvanostatic charge/discharge tests were conducted on a LANHE electrochemical workstation with a potential window of 0.01−3.00 V (vs Li^+/Li). Cyclic voltammetry (CV) and electrochemical impedance spectroscopy (EIS) measurements were conducted at the EC-Lab electrochemical workstation. CV was tested at a scan rate of 0.2 mV s^{-1} in a voltage range of 0.01−3.00 V. The CV of $NiFe_2O_4$/rGO at various scan rates was also tested in a voltage range of 0.01−3.00 V. In the EIS measurement, the amplitude of the AC signal is 0.2 mV and the frequency is between 100 kHz and 0.01 Hz.

■ ASSOCIATED CONTENT

Supporting Information

The Supporting Information is available free of charge at https://pubs.acs.org/doi/10.1021/acsomega.1c03050.

Raman spectra of $NiFe_2O_4$ (black line) and $NiFe_2O_4$/rGO (red line) (Figure S1); TGA curve for $NiFe_2O_4$/rGO (Figure S2); TEM images of $NiFe_2O_4$ (a, b, and c) and SAED pattern of $NiFe_2O_4$ (d) (Figure S3); EDS spectrum of $NiFe_2O_4$/rGO (Figure S4); and charge/discharge capacity and Coulombic efficiency of the $NiFe_2O_4$ electrode (Figure S5). The calculation of lithium-ion diffusion coefficients has been listed on page S7 (PDF)

■ AUTHOR INFORMATION

Corresponding Author

Kun Luo − *Key Laboratory of Advanced Energy Materials Chemistry (Ministry of Education), Renewable Energy Conversion and Storage Center, College of Chemistry, Nankai University, Tianjin 300071, P. R. China;* orcid.org/0000-0002-5754-0222; Email: kun.luo@nankai.edu.cn

Authors

Chang Liu − *Key Laboratory of Advanced Energy Materials Chemistry (Ministry of Education), Renewable Energy Conversion and Storage Center, College of Chemistry, Nankai University, Tianjin 300071, P. R. China*

Tong Zhang − *Key Laboratory of Advanced Energy Materials Chemistry (Ministry of Education), Renewable Energy Conversion and Storage Center, College of Chemistry, Nankai University, Tianjin 300071, P. R. China*

Lixin Cao − *Key Laboratory of Advanced Energy Materials Chemistry (Ministry of Education), Renewable Energy Conversion and Storage Center, College of Chemistry, Nankai University, Tianjin 300071, P. R. China*

Complete contact information is available at: https://pubs.acs.org/10.1021/acsomega.1c03050

Notes

The authors declare no competing financial interest.

■ ACKNOWLEDGMENTS

This study was supported by the Key Laboratory of Advanced Energy Materials Chemistry, Renewable Energy Conversion and Storage Center, College of Chemistry, Nankai University.

■ REFERENCES

(1) Kang, K.; Meng, Y. S.; Bréger, J.; Grey, C. P.; Ceder, G. Electrodes with High Power and High Capacity for Rechargeable Lithium Batteries. *Science* **2006**, *311*, 977.
(2) Roy, P.; Srivastava, S. K. Nanostructured anode materials for lithium ion batteries. *J. Mater. Chem. A* **2015**, *3*, 2454−2484.
(3) Tarascon, J. M.; Armand, M. Issues and challenges facing rechargeable lithium batteries. *Nature* **2001**, *414*, 359−367.
(4) Song, S. C.; Zuo, D. C.; An, C. S.; Zhang, X. H.; Li, J. H.; He, Z. J.; Li, Y. J.; Zheng, J. C. Self-assembled GeOX/Ti3C2TX Composites as Promising Anode Materials for Lithium Ion Batteries. *Inorg. Chem.* **2020**, *59*, 4711−4719.
(5) Cheng, X.-B.; Zhang, R.; Zhao, C.-Z.; Zhang, Q. Toward Safe Lithium Metal Anode in Rechargeable Batteries: A Review. *Chem. Rev.* **2017**, *117*, 10403−10473.
(6) Liu, J.; Bao, Z.; Cui, Y.; Dufek, E. J.; Goodenough, J. B.; Khalifah, P.; Li, Q.; Liaw, B. Y.; Liu, P.; Manthiram, A.; Meng, Y. S.; Subramanian, V. R.; Toney, M. F.; Viswanathan, V. V.; Whittingham, M. S.; Xiao, J.; Xu, W.; Yang, J.; Yang, X.-Q.; Zhang, J.-G. Pathways for practical high-energy long-cycling lithium metal batteries. *Nat. Energy* **2019**, *4*, 180−186.
(7) Armand, M.; Tarascon, J. M. Building better batteries. *Nature* **2008**, *451*, 652−657.
(8) Ding, B.; Cai, Z.; Ahsan, Z.; Ma, Y.; Zhang, S.; Song, G.; Yuan, C.; Yang, W.; Wen, C. A Review of Metal Silicides for Lithium-Ion Battery Anode Application. *Acta Metall. Sin.* **2021**, *34*, 291−308.
(9) Zheng, C.; Zeng, L.; Wang, M.; Zheng, H.; Wei, M. Synthesis of hierarchical ZnV2O4 microspheres and its electrochemical properties. *CrystEngComm* **2014**, *16*, 10309−10313.
(10) Poizot, P.; Laruelle, S.; Grugeon, S.; Dupont, L.; Tarascon, J. M. Nano-sized transition-metal oxides as negative-electrode materials for lithium-ion batteries. *Nature* **2000**, *407*, 496−499.
(11) Hao, Q.; Lei, D.; Yin, X.; Zhang, M.; Liu, S.; Li, Q.; Chen, L.; Wang, T. 3-D mesoporous nano/micro-structured Fe3O4/C as a superior anode material for lithium-ion batteries. *J. Solid State Electrochem.* **2011**, *15*, 2563−2569.
(12) Zhu, K.; Zhang, Y.; Qiu, H.; Meng, Y.; Gao, Y.; Meng, X.; Gao, Z.; Chen, G.; Wei, Y. Hierarchical Fe3O4 microsphere/reduced graphene oxide composites as a capable anode for lithium-ion batteries with remarkable cycling performance. *J. Alloys Compd.* **2016**, *675*, 399−406.
(13) Yue, Y.; Liang, H. Micro- and Nano-Structured Vanadium Pentoxide (V2O5) for Electrodes of Lithium-Ion Batteries. *Adv. Energy Mater.* **2017**, *7*, No. 1602545.
(14) Lu, S. J.; Wang, Z. T.; Zhang, X. H.; He, Z. J.; Tong, H.; Li, Y. J.; Zheng, J. C. In Situ-Formed Hollow Cobalt Sulfide Wrapped by Reduced Graphene Oxide as an Anode for High-Performance Lithium-Ion Batteries. *ACS Appl. Mater. Interfaces* **2020**, *12*, 2671−2678.
(15) Liu, L.; Yu, Y.; Yan, C.; Li, K.; Zheng, Z. Wearable energy-dense and power-dense supercapacitor yarns enabled by scalable graphene−metallic textile composite electrodes. *Nat. Commun.* **2015**, *6*, No. 7260.
(16) Lian, C.; Wang, Z.; Lin, R.; Wang, D.; Chen, C.; Li, Y. An efficientfficient, controllable and facile two-step synthesis strategy: Fe3O4@RGO composites with various Fe3O4 nanoparticles and their supercapacitance properties. *Nano Res.* **2017**, *10*, 3303−3313.
(17) Tang, L. B.; Zhang, B.; An, C. S.; Li, H.; Xiao, B.; Li, J. H.; He, Z. J.; Zheng, J. C. Ultrahigh-Rate Behavior Anode Materials of MoSe2 Nanosheets Anchored on Dual-Heteroatoms Functionalized Graphene for Sodium-Ion Batteries. *Inorg. Chem.* **2019**, *58*, 8169−8178.
(18) Zhou, Y.; Li, Y.; Wang, Q.; Wang, Q.; Du, R.; Zhang, M.; Sun, X.; Zhang, X.; Kang, L.; Jiang, F. Ultrasmall MoS3 Loaded GO Nanocomposites as High-Rate and Long-Cycle-Life Anode Materials for Lithium- and Sodium-Ion Batteries. *ChemElectroChem* **2019**, *6*, 3113−3119.
(19) Chen, X. Q.; Lin, H. B.; Zheng, X. W.; Cai, X.; Xia, P.; Zhu, Y. M.; Li, X. P.; Li, W. S. Fabrication of core−shell porous nanocubic Mn2O3@TiO2 as a high-performance anode for lithium ion batteries. *J. Mater. Chem. A* **2015**, *3*, 18198−18206.
(20) Alcántara, R.; Jaraba, M.; Lavela, P.; Tirado, J. L.; Jumas, J. C.; Olivier-Fourcade, J. Changes in oxidation state and magnetic order of iron atoms during the electrochemical reaction of lithium with NiFe2O4. *Electrochem. Commun.* **2003**, *5*, 16−21.
(21) Park, G. D.; Cho, J. S.; Kang, Y. C. Multiphase and Double-Layer NiFe2O4@NiO-Hollow-Nanosphere-Decorated Reduced Graphene Oxide Composite Powders Prepared by Spray Pyrolysis Applying Nanoscale Kirkendall Diffusion. *ACS Appl. Mater. Interfaces* **2015**, *7*, 16842−16849.
(22) Liu, H.; Zhu, H.; Yang, H. A low temperature synthesis of nanocrystalline spinel NiFe2O4 and its electrochemical performance as anode of lithium-ion batteries. *Mater. Res. Bull.* **2013**, *48*, 1587−1592.
(23) Lavela, P.; Tirado, J. L. CoFe2O4 and NiFe2O4 synthesized by sol−gel procedures for their use as anode materials for Li ion batteries. *J. Power Sources* **2007**, *172*, 379−387.
(24) Li, S.; Li, A.; Zhang, R.; He, Y.; Zhai, Y.; Xu, L. Hierarchical porous metal ferrite ball-in-ball hollow spheres: General synthesis, formation mechanism, and high performance as anode materials for Li-ion batteries. *Nano Res.* **2014**, *7*, 1116−1127.
(25) Cherian, C. T.; Sundaramurthy, J.; Reddy, M. V.; Suresh Kumar, P.; Mani, K.; Pliszka, D.; Sow, C. H.; Ramakrishna, S.; Chowdari, B. V. R. Morphologically Robust NiFe2O4 Nanofibers as High Capacity Li-Ion Battery Anode Material. *ACS Appl. Mater. Interfaces* **2013**, *5*, 9957−9963.
(26) Heidari, E. K.; Zhang, B.; Sohi, M. H.; Ataie, A.; Kim, J.-K. Sandwich-structured graphene−NiFe2O4−carbon nanocomposite anodes with exceptional electrochemical performance for Li ion batteries. *J. Mater. Chem. A* **2014**, *2*, 8314−8322.
(27) Dong, T.; Wang, G.; Yang, P. Electrospun NiFe2O4@C fibers as high-performance anode for lithium-ion batteries. *Diamond Relat. Mater.* **2017**, *73*, 210−217.
(28) Choi, M.; Koppala, S. K.; Yoon, D.; Hwang, J.; Kim, S. M.; Kim, J. A route to synthesis molybdenum disulfide-reduced graphene oxide (MoS2-RGO) composites using supercritical methanol and their enhanced electrochemical performance for Li-ion batteries. *J. Power Sources* **2016**, *309*, 202−211.
(29) Li, F.; Zhang, L.; Li, J.; Lin, X.; Li, X.; Fang, Y.; Huang, J.; Li, W.; Tian, M.; Jin, J.; Li, R. Synthesis of Cu−MoS2/rGO hybrid as non-noble metal electrocatalysts for the hydrogen evolution reaction. *J. Power Sources* **2015**, *292*, 15−22.
(30) Xu, Z. L.; Zhang, B.; Zhou, Z. Q.; Abouali, S.; Akbari Garakani, M.; Huang, J.; Huang, J. Q.; Kim, J. K. Carbon nanofibers containing Si nanoparticles and graphene-covered Ni for high performance anodes in Li ion batteries. *RSC Adv.* **2014**, *4*, 22359−22366.
(31) Liu, Y.; Zhang, N.; Yu, C.; Jiao, L.; Chen, J. MnFe2O4@C Nanofibers as High-Performance Anode for Sodium-Ion Batteries. *Nano Lett.* **2016**, *16*, 3321−3328.
(32) Bakhshi, H.; Mohammad Azari, M.; Shokuhfar, A. A facile approach for obtaining NiFe2O4@C core-shell nanoparticles and their magnetic properties assessment. *Diamond Relat. Mater.* **2020**, *110*, No. 108159.
(33) D'Ippolito, V.; Andreozzi, G. B.; Bersani, D.; Lottici, P. P. Raman fingerprint of chromate, aluminate and ferrite spinels. *J. Raman Spectrosc.* **2015**, *46*, 1255−1264.
(34) Paswan, S. K.; Kumari, S.; Kar, M.; Singh, A.; Pathak, H.; Borah, J. P.; Kumar, L. Optimization of structure-property relationships in nickel ferrite nanoparticles annealed at different temperature. *J. Phys. Chem. Solids* **2021**, *151*, No. 109928.
(35) Sousa, M. H.; Tourinho, F. A.; Rubim, J. C. Use of Raman micro-spectroscopy in the characterization of MIIFe2O4 (M = Fe,

https://doi.org/10.1021/acsomega.1c03050
ACS Omega 2021, 6, 25269−25276

Zn) electric double layer ferrofluids. *J. Raman Spectrosc.* **2000**, *31*, 185−191.
(36) Fu, M.; Qiu, Z.; Chen, W.; Lin, Y.; Xin, H.; Yang, B.; Fan, H.; Zhu, C.; Xu, J. NiFe2O4 porous nanorods/graphene composites as high-performance anode materials for lithium-ion batteries. *Electrochim. Acta* **2017**, *248*, 292−298.
(37) Zhao, J.; Li, X.; Cui, G.; Sun, X. Highly-active oxygen evolution electrocatalyzed by an Fe-doped NiCr2O4 nanoparticle film. *Chem. Commun.* **2018**, *54*, 5462−5465.
(38) Chen, Q.; Wang, R.; Lu, F.; Kuang, X.; Tong, Y.; Lu, X. Boosting the Oxygen Evolution Reaction Activity of NiFe2O4 Nanosheets by Phosphate Ion Functionalization. *ACS Omega* **2019**, *4*, 3493−3499.
(39) Huang, X. H.; Tu, J. P.; Zhang, B.; Zhang, C. Q.; Li, Y.; Yuan, Y. F.; Wu, H. M. Electrochemical properties of NiO−Ni nanocomposite as anode material for lithium ion batteries. *J. Power Sources* **2006**, *161*, 541−544.
(40) Gao, X.; Wang, J.; Zhang, D.; Nie, K.; Ma, Y.; Zhong, J.; Sun, X. Hollow NiFe2O4 nanospheres on carbon nanorods as a highly efficient anode material for lithium ion batteries. *J. Mater. Chem. A* **2017**, *5*, 5007−5012.
(41) Zhu, J.; Yang, D.; Rui, X.; Sim, D.; Yu, H.; Hoster, H. E.; Ajayan, P. M.; Yan, Q. Facile Preparation of Ordered Porous Graphene−Metal Oxide@C Binder-Free Electrodes with High Li Storage Performance. *Small* **2013**, *9*, 3390−3397.
(42) Cho, J. S.; Hong, Y. J.; Kang, Y. C. Design and Synthesis of Bubble-Nanorod-Structured Fe2O3−Carbon Nanofibers as Advanced Anode Material for Li-Ion Batteries. *ACS Nano* **2015**, *9*, 4026−4035.
(43) Fu, Y.; Wan, Y.; Xia, H.; Wang, X. Nickel ferrite−graphene heteroarchitectures: Toward high-performance anode materials for lithium-ion batteries. *J. Power Sources* **2012**, *213*, 338−342.
(44) Zheng, T.; Gozdz, A. S.; Amatucci, G. G. Reactivity of the Solid Electrolyte Interface on Carbon Electrodes at Elevated Temperatures. *J. Electrochem. Soc.* **1999**, *146*, 4014−4018.
(45) Chen, C. H.; Hwang, B. J.; Do, J. S.; Weng, J. H.; Venkateswarlu, M.; Cheng, M. Y.; Santhanam, R.; Ragavendran, K.; Lee, J. F.; Chen, J. M.; Liu, D. G. An understanding of anomalous capacity of nano-sized CoO anode materials for advanced Li-ion battery. *Electrochem. Commun.* **2010**, *12*, 496−498.
(46) Yuan, F.-W.; Yang, H.-J.; Tuan, H.-Y. Alkanethiol-Passivated Ge Nanowires as High-Performance Anode Materials for Lithium-Ion Batteries: The Role of Chemical Surface Functionalization. *ACS Nano* **2012**, *6*, 9932−9942.
(47) Zhang, Y.; Cao, W.; Cai, Y.; Shu, J.; Cao, M. Rational design of NiFe2O4−rGO by tuning the compositional chemistry and its enhanced performance for a Li-ion battery anode. *Inorg. Chem. Front.* **2019**, *6*, 961−968.
(48) Chen, Y.; Zhu, J.; Qu, B.; Lu, B.; Xu, Z. Graphene improving lithium-ion battery performance by construction of $NiCo_2O_4$/graphene hybrid nanosheet arrays. *Nano Energy* **2014**, *3*, 88−94.

https://doi.org/10.1021/acsomega.1c03050
ACS Omega 2021, 6, 25269−25276